Additive Manufacturing of Tailored Macroporous Ceramic Structures for High-Temperature Applications

Sadaf Sobhani, Shawn Allan, Priyanka Muhunthan, Emeric Boigne, and Matthias Ihme*

Macroporous ceramic materials are ubiquitous in numerous energy-conversion and thermal-management systems. The morphology and material composition influence the effective thermophysical properties of macroporous ceramic structures and interphase transport in interactions with the working fluid. Therefore, tailoring these properties can enable significant performance enhancements by modulating thermal transport, reactivity, and stability. However, conventional ceramic-matrix fabrication techniques limit the ability for tailoring the porous structure and optimizing the performance of these systems, such as by introducing anisotropic morphologies, pore-size gradations, and variations in pore connectivity and material properties. Herein, an integrated framework is proposed for enabling the design, optimization, and fabrication of tailored ceramic porous structures by combining computational modeling, mathematically defined surfaces, and lithography-based additive manufacturing. The benefits of pore-structure tailoring are illustrated experimentally for interstitial combustion in a porous-media burner operating with a smoothly graded matrix structure. In addition, a remarkable range of achievable thermal conductivities for a single material is demonstrated with tuning of the fabrication process, thus providing unique opportunities for modulating thermal transport properties of porous-ceramic structures.

The excellent thermal properties and corrosion resistance make porous ceramic structures attractive for a wide range of technical applications, such as solar receivers, catalytic converters, reformers, heat exchangers, porous-media burners (PMBs), thermal protection, and transpiration cooling materials in hypersonic applications[1–4] (see **Figure 1** for representative examples).

Dr. S. Sobhani
Sibley School of Mechanical and Aerospace Engineering
Cornell University
Ithaca, NY 14853, USA
E-mail: sobhani@cornell.edu

Dr. S. Sobhani, P. Muhunthan, E. Boigne, Prof. M. Ihme
Department of Mechanical Engineering
Stanford University
Stanford, CA 94305, USA

S. Allan
Lithoz America LLC
Troy, NY 12180, USA

The ORCID identification number(s) for the author(s) of this article can be found under https://doi.org/10.1002/adem.202000158.

Various high-performance ceramic materials are utilized in these technical applications, including alumina (Al_2O_3), yttria-stabilized zirconia alumina (YZA), and silicon carbide (SiC). Al_2O_3 enables the highest maximum use temperature, but has intermediate resistance to thermal shock, whereas SiC has superior thermal shock resistance and thermal conductivity, but lower usage temperature. Thus, different properties metrics determine the application of the material for high-temperature applications.[5]

In addition to the material composition, the local porous structure directly affects global properties such as total heat transfer across a porous material or heat exchange between the working fluid and the solid structure. Therefore, the ability for tailoring the structure is critical for numerous applications. Traditional ceramic fabrication methods involving pressing or casting result in dense, low-porosity materials. Therefore, manufacturing highly porous structures with controlled porosity requires the use of special manufacturing techniques. Such techniques primarily rely on the replication of a high-porosity polymer or carbon structure either by coating with a ceramic slurry or by vapor deposition.[6] Alternatively, highly porous ceramic materials can be produced by foaming methods, which incorporate a gas into a suspension that subsequently sets to maintain the structure of the bubbles.[7] These techniques are not directly amenable to the tailoring of the local porous structure, thus enabling structural tailoring for optimizing the system performance necessitates the use of advanced manufacturing techniques, such as additive manufacturing (AM). AM allows for the fabrication of highly complex and tailored structures from computer-aided design (CAD) model data. However, the high-melting temperatures of ceramics have made them specially challenging for AM, with only a few technologies capable of converting a digital representation to a physical ceramic structure. An additional challenge to creating complex porous ceramic structures is resolving the sub-millimeter pore and strut features, which are relevant for practical applications. Leveraging the technologies available for polymer AM, previous studies have applied customized template-polymer structures in the traditional replication methodology to enable tailored ceramic structures.[8] However, the replication method relies on the burnout of the underlying template
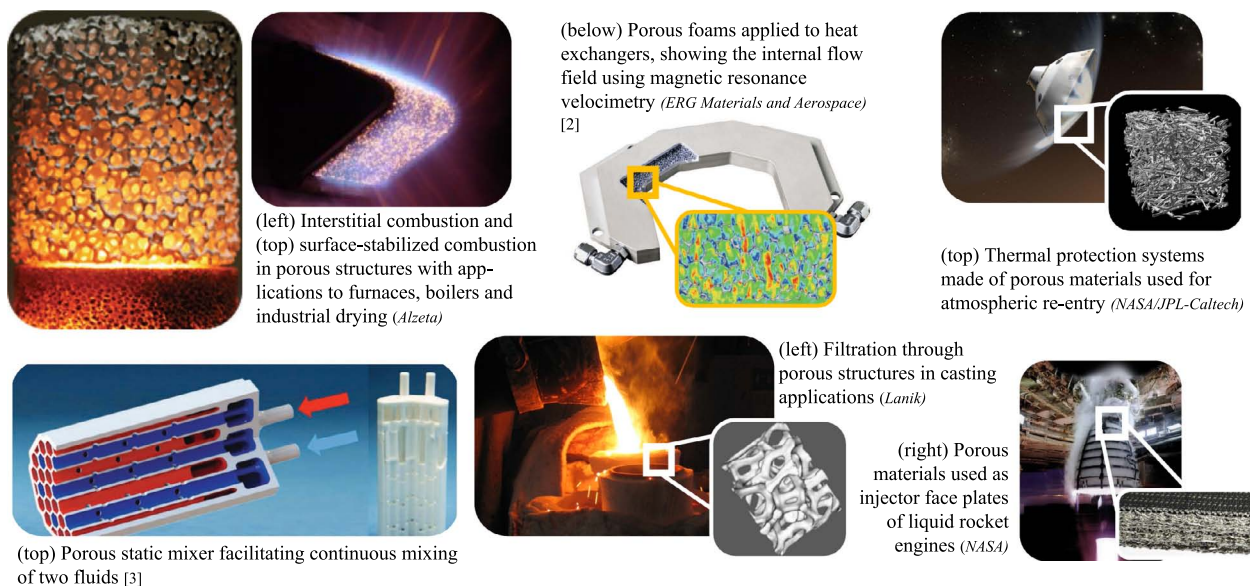
Figure 1. Application of macroporous ceramic structures in high-temperature and corrosive environments.

structure, resulting in hallow struts that adversely affect the thermomechanical properties of the final product.[6]

AM methods capable of producing dense ceramic parts are divided into direct and indirect techniques.[9] Direct techniques are powder-based and use thermal energy input by a laser to selectively melt or sinter the ceramic grains to form the final part. In contrast, indirect techniques first print a so-called "green part" that consist of ceramic particles and an organic binder, which is then thermally treated to remove the organic components and sinter the ceramic grains. Lithography-based methods are a subset of indirect techniques that rely on selective space-resolved exposure to light to solidify the liquid suspension. In digital light processing (DLP), a part is created from a suspension of ceramic particles in a photosensitive resin, which is shaped via photochemical reactions. Photopolymerization-based technologies, such as DLP, enable significantly higher feature resolution and surface quality as compared with thermal energy-based methods, such as selective laser sintering.[10]

In this study, a framework is proposed to design and fabricate, using DLP lithography-based ceramic manufacturing (LCM), tailored ceramic porous structures for application to high-temperature environments. This framework, as summarized in **Figure 2**, is demonstrated in application to PMBs by designing, manufacturing, and experimentally verifying performance gains of smoothly graded matrix structures for high-temperature combustion environments. With relevance to tailoring macro-thermal properties and structural durability, the printed samples were analyzed to characterize the effects of feedstock particle diameter, layer thickness, and printing orientation of LCM alumina. Scanning electron microscope (SEM) and energy dispersive X-ray (EDX) analysis techniques were used to characterize material degradation and chemical changes. Finally, micro-X-ray computed tomography (μ-XCT) imaging was used to examine the fidelity of the printing technology in reproducing the input stereolithography (STL) geometry.

So far, gradation of porous ceramic morphology for high-temperature applications was only achieved by stacking segments of conventionally manufactured ceramic foams of different discrete pore sizes or porosities and then sintering to create a final part. To leverage recent advances in AM for fabricating smoothly graded porous structures, a design methodology is required to create a digital rendering of the desired structure in a format compatible with the LCM printers. In this work, the morphology of the porous structure used as input to the printer is designed using geometric surface equations. These mathematically defined surfaces are ideal for enabling the 3D control of the porous structure. The matrix unit type used in this study is based on a subset of periodic surface equations, known as triply periodic minimal surfaces (TPMS). TPMS offer several advantages over strut-based lattice structures, including high surface-to-volume ratio, enhanced pore connectivity, and ease of functional grading.[11] These surfaces provide a versatile framework for designing porous structures with tailored properties. While these surface geometries have been utilized primarily in bone and tissue engineering,[12–14] the novelty of this work consists in using these geometric representations in the design of porous ceramic structures with tailored properties for application to high-temperature and corrosive environments. The topologically simplest forms of TPMS that have cubic lattice symmetry are the primitive (P), gyroid (G), and diamond (D) surfaces.[15,16] As an illustrative example, this study considers a diamond lattice structure

$$F_D(\boldsymbol{x}) = \sin\left(\sum_{i=1}^{3} \omega_i(z) x_i\right) + 2 \prod_{i=1}^{3} \sin(\omega_i(z) x_i) + q(z) \tag{1}$$

where $\boldsymbol{x} = (x, y, z)^T$ is the spatial coordinate vector with z corresponding to the axial direction, and the parameters describing the wavelength, $\boldsymbol{\omega} = (\omega_x, \omega_y, \omega_z)^T$, and the compaction, q, is modified to introduce a spatial gradation along the axial direction. In the following, in-plane homogeneity is assumed, implying
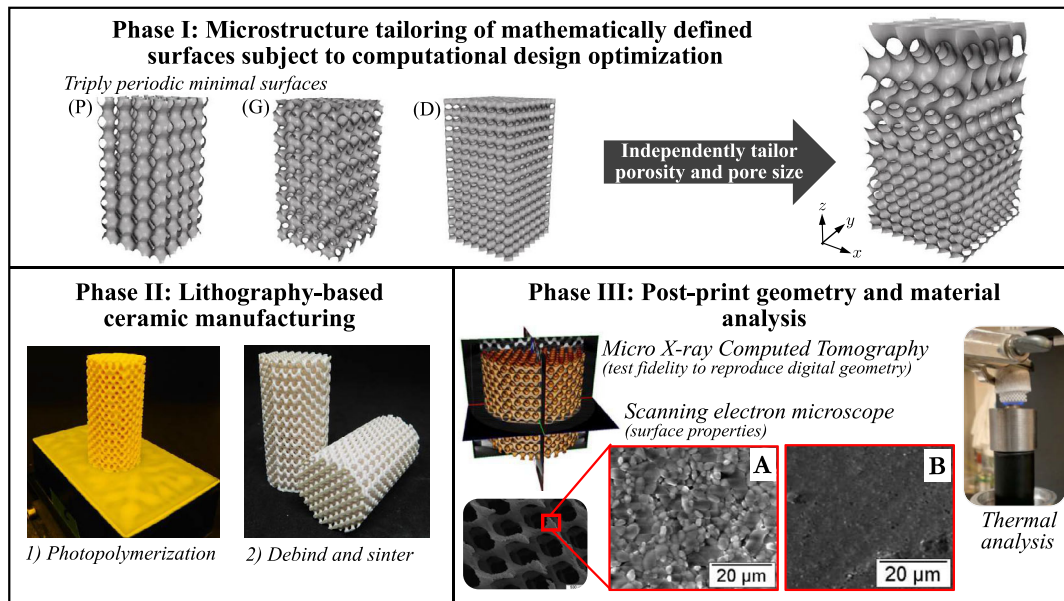
2000158 (2 of 8)

Figure 2. Schematic outlining the three phases of actualizing tailored porous structures, starting from design using mathematically defined surfaces, fabrication, and post-print analysis. SEM images in bottom right image illustrate variations in surface roughness and microporosity of different sinter materials used in this study.

$\omega = \omega_i$. The void space is defined by $F_D > 0$; thus, an equivalent porosity $\epsilon_{eq}(z)$ of the macroporous ceramic matrix can be calculated as follows

$$\epsilon_{eq}(z) = \frac{1}{A} \iiint G_\Delta(z - z') \mathcal{H}(F(\boldsymbol{x}'))d\boldsymbol{x}' \tag{2}$$

where A is the cross-sectional area, $\mathcal{H}$ is the Heaviside function, and G_Δ is a Gaussian filter kernel with filter width Δ: $G_\Delta(\zeta) = \exp\{-\zeta^2/(2\Delta^2)\}/(\sqrt{2\pi}\Delta)$.

The equivalent pore diameter is then computed as

$$d_{eq}(z) = \left[\frac{4\epsilon_{eq}(z)A}{\pi N_p(z)}\right]^{1/2} \tag{3}$$

where N_p is the total number of pores in cross-sectional area A.

By considering $\boldsymbol{\omega}$ and q as design variables, the morphology of the macroporous ceramic matrix structure can be formulated as a generalized optimization problem

$$\begin{aligned} \underset{\omega, q}{\text{minimize}} \quad & f(\omega, q) \\ \text{subject to} \quad & \{\mathcal{M}, \mathcal{C}\} \end{aligned} \tag{4}$$

where f denotes the objective function of choice, such as pressure drop pollutant, chemical conversion rate, or other performance criteria that can be evaluated computationally.[17] Physical limitations that are introduced by the LCM process (such as maximum print resolution and part size, over-polymerization effects, etc.) and constraints on performance (including thermal stresses, stability, and structural properties) are denoted by the functionals $\mathcal{M}$ and $\mathcal{C}$, respectively. Multiparametric optimization techniques in conjunction with computational models that describe the system performance can be used to solve this optimization problem.[18,19] Once the desired geometry is obtained,

an isosurface of the lattice structure is created and converted to an STL geometry for input to the printer system.

In this study, the DLP LCM technique is used to demonstrate the fabrication of tailored macroporous ceramic structures.[9] The advantages of this method, as compared with direct powder-based techniques, are higher feature resolution and surface quality,[10] and achieving ceramic components with significantly higher density (>99%), which, in turn, enables equivalent strength properties as products from conventional methods, such as injection molding or dry pressing, but with significantly greater geometric flexibility.[20]

Prior to printing, the geometry is first modified to address over-polymerization within the layers (x–y plane) and across the layers (along the z-printing direction), respectively. To ensure adhesion between exposed layers, the curing depth is set two to four times larger than the layer thickness. However, this has the undesired effect of over-polymerization along the z-printing direction (i.e., light curing of regions where no curing was planned). To correct this, light exposure to certain features is delayed to offset effects related to the penetration of light through the slurry between layers. Over-polymerization can simultaneously affect the x–y plane, due to light scattering in the slurry.[21] To compensate for these effects, features are enlarged or shrunk (i.e., by adding or removing pixels around the feature). After the digital file is corrected for over-polymerization, it is then scaled up by a factor of 1.22 in the x- and y-directions and by a factor of 1.28 in the z-direction to compensate for the shrinkage during sintering.[9]

In this study, a CeraFab 7500 printer was used, which uses blue light-emitting diodes and a digital light projector to create an array of 40 μm pixels over a 76×43 mm^2 area. Each layer was produced by illuminating the slice image, using a monochromatic (450 nm) projector, into the vat of slurry, with a

**ADVANCED
SCIENCE NEWS**
www.advancedsciencenews.com

**ADVANCED
ENGINEERING
MATERIALS**
www.aem-journal.com

slurry depth of $\approx$250 µm. The light penetration depth was equal to 200 µm to ensure good adhesion between the layers. Samples were printed in layers with 25 or 50 µm thickness, first producing a 3D composite of photopolymer and ceramic powder in a green part. The green part was then removed from the printer for postprocessing, where excess slurry was cleaned from the parts with the use of a cleaning solution (LithaSol 20, Lithoz GmbH), compressed air, and an ultrasonic bath. Cleaning is critical for removing excess slurry that is retained in the matrix structures by capillary forces. The green part was then thermally processed to remove the organic material and subsequently sintered to form the final ceramic part.

The printer functions with the same principle as STL and DLP systems for printing polymers using selective space-resolved exposure to light to solidify a liquid resin. In LCM, however, the liquid contains a homogeneous suspension of ceramic particles, which result in additional challenges in the fabrication process due to light scattering, agglomeration, and settling of the fine particles. Previous studies have investigated the role of various binder polymers to control the rheological behavior of the suspension as well as the structural properties of the final part.[22] In this study, two different grades of commercially available suspensions were used (LithaLox, Lithoz GmbH). LithaLox 350D (material A) consists of 99.8% Al_2O_3 and powder particle sizes between 0.5 and 1 µm that sinter together to $\approx$98% density. LithaLox HP500 (material B) is a suspension with 99.99% Al_2O_3 and particle sizes between 0.1 and 0.5 µm that sinter to form over 99.4% density. The other distinguishing feature between the two suspensions is the surface roughness of the final product, which is reported by the manufacturer as 0.4 µm for HP500 and 0.9 µm for 350D. The variation in surface roughness and microporosity are evident in the SEM images in Figure 2, which were taken using an XL30 environmental SEM.

As the local morphology of the macroporous ceramic structure directly influences the thermal and transport properties of the porous system, the accuracy of the LCM technique in actualizing a digital design is critical. With specific focus on examining challenges arising from printing spatially graded porous structures that arise from variations in feature size within the same part, a structure with linear variation in equivalent pore diameter and porosity was examined. To this end, the optimization problem was solved subject to the following cost-function constraints

$$d_{eq}(z) = d_{eq,1} + (d_{eq,2} - d_{eq,1})\frac{z}{L} \tag{5}$$

$$\epsilon_{eq}(z) = \epsilon_{eq,1} + (\epsilon_{eq,2} - \epsilon_{eq,1})\frac{z}{L} \tag{6}$$

where L is the axial length of the sample, and subscripts 1 and 2 refer to the limits of the parameter within the sample. With these constraints, TPMS parameters $\omega(z)$ and $q(z)$ are obtained as solution to the optimization problem of Equation (4). In this work, two different pore morphologies are considering, and corresponding quantities for equivalent pore diameter, equivalent porosity, and TPMS parameters are summarized in **Table 1**.

The μ-XCT image analysis is used to compare the 3D features of the printed parts to those of the input data. ZEISS Xradia 520 Versa X-ray microscope scanner is used with a 80 kVp and 90 mA X-ray beam and a voxel size of 12 µm to fully resolve the finest

Table 1. Parameters for the macroporous matrix morphologies considered in this study.

Morphology	$(d_{eq,1}, d_{eq,2})$ [mm]	$(\epsilon_{eq,1}, \epsilon_{eq,2})$	(ω_1, ω_2) [mm^{-1}]	(q_1, q_2)
Graded pore size	(1.5,3.5)	(0.75, 0.75)	(2.0165, 4.7155)	(0.5045, 0.5045)
Graded porosity	(2.5, 2.5)	(0.65, 0.85)	(2.8320, 2.8145)	(0.2890, 0.7540)

features of the porous structure that are associated with the DLP-layer thickness ($\approx$25 µm). Morphological features were evaluated along the axial direction of the cylindrical ceramic pieces. The structure of porous matrix consists of polyhedra (cell diameter) connected by openings or windows (window diameter). As opposed to computing an equivalent pore diameter using Equation (3), the void space is quantified by the window and cell diameters to provide additional details about the porous structure. Using a 3D distance transform watershed algorithm followed by a 3D particle analyzer performed on the gas domain,[23,24] the cell diameters were computed by representing each cell with a sphere of equivalent volume, whereas the window diameters were obtained as the diameters of the circles of equivalent areas. The strut throats, defined as the thinnest part of the struts, were extracted by applying the same algorithms on the solid domain. Porosity was estimated as the ratio of gas voxels over the total number of voxels at each axial position. This methodology was applied to the μ-XCT images of the final parts as well as their STL geometries to facilitate comparisons. Results from this analysis are presented in **Figure 3** for the graded pore-size matrix. The actual output cell and window diameters show excellent agreement with those of the input structure, exhibiting only a minor overshoot in regions with the smallest strut features. The mean throat diameter in four cells shown in Figure 3 is evaluated as 352 µm for the input geometry, versus 229 µm for the 3D printed sample. Although this variation does not correspond to significant changes in the cell or window size, discrepancies are found between the porosity profiles that become more pronounced with decreasing feature size. This is due to thinner features absorbing less light than thicker ones at equivalent curing energies, and, therefore, become thinner than that prescribed by the input STL geometry. To alleviate this effect, in addition to the preprocessing previously described, the input geometry should also be modified to account for strut thinning in graded porous structures.

Beyond identifying the fidelity of the LCM technique in reproducing the desired morphology, the influence of the fabrication parameters on thermal conductivity is analyzed. Disk samples of each material (A: 350D, B: HP500) were printed to experimentally characterize the effects of printing layer thickness and material composition on the effective thermal conductivity. The solid disks tested had a diameter of 25 mm and a height of 5 mm. Samples were manufactured by printing layers along the x–y plane, parallel to the face of the disk. Samples printed perpendicular to the face of the disk were also examined; however, the thermal conductivity measured for these samples was found to exceed the capacity of the instrument to produce reliable quantitative measurements. Therefore, the data presented correspond only to samples printed along the x–y plane, with thermal
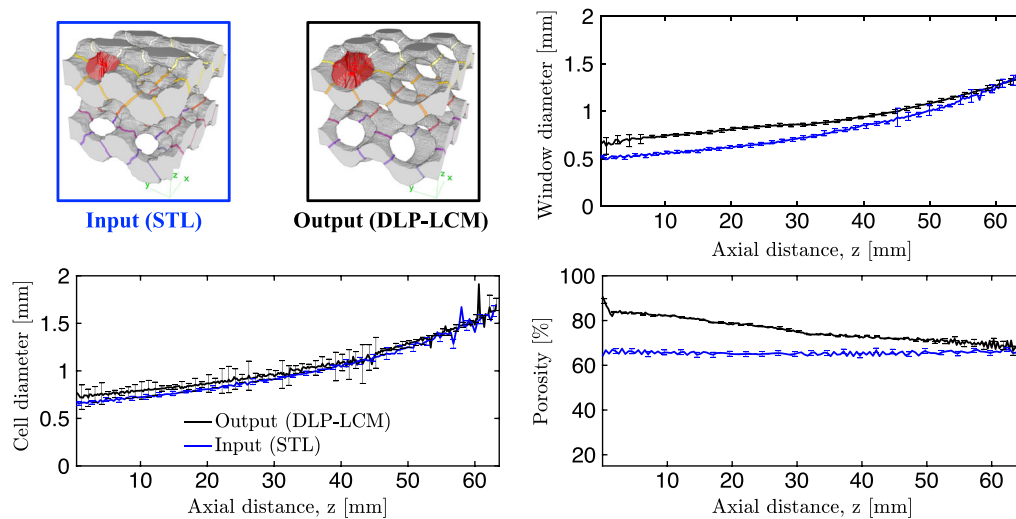
Figure 3. Post-print analysis of macroporous ceramic matrix morphology with axially graded pore size using μ-XCT at a spatial resolution of 12 μm, showing variations between the designed (blue) and actual (black) porous matrix with error bars along with volume renderings of four cells within the solid matrix; red surfaces denote the openings or windows of the matrix. Colored rings on the struts indicate the throat locations.

conductivity measured in the *z*-direction. The samples were printed with two different layer thicknesses, i.e., 25 and 50 μm.

The thermal conductivity of the samples was characterized with the C-Therm TCi analyzer using the modified transient plane source method.[25] Thermal conductivity measurements were performed at 298, 373, and 473 K, with distilled water as the contact agent for tests at 298 K and Wakefield 120 Thermal Grease at elevated temperatures. Each reported test result is the average of five measurements, which was then repeated three times for a total of 15 tests per sample. The averaged values of the three measurements are shown in **Figure 4**a. The maximum standard deviation was 1.6%. To quantify the effects imposed by the LCM-fabrication technique, the thermal conductivity of conventionally manufactured high-grade alumina is also shown, as evaluated using the following expression[26]

$$\frac{\lambda_{s,\text{conv}}}{\lambda_{s,\text{conv}}^0} = 0.15 + 2.311 \exp\{-T/T_0\} \tag{7}$$

where $T_0 = 303$ K and $\lambda_{s,\text{conv}}^0 = 36.75$ W m^{-1} K^{-1}. Figure 4a shows that the thermal conductivity of LCM-fabricated samples is lower than that of the common high-grade alumina ceramics prepared by conventional approaches.[26] This discrepancy originates from the specific nature of the LCM fabrication technique as well as the effectiveness of the layer-to-layer adhesion and material density by particle–particle sintering.

At ambient conditions, the high-density material B (HP500) has higher thermal conductivity than material A, and a reduction in conductivity is observed between the conventional and LCM alumina by 89.2% for A, 25 μm and 32.1% for A, 50 μm. This reduction is less pronounced and nearly independent of layer thickness for material B, with a change of 23.8% for B, 25 μm and 22.7% for B, 50 μm. Thus, larger particles combined with thin print layers enable the lowest thermal conductivity, whereas smaller particles independent of layer thickness result in the highest thermal conductivity. These dependencies on the

sintering material and layering indicate significant potential for tailoring the local thermal conductivity by tuning the fabrication process. Variations between the conventional and LCM alumina increase with temperature for all four sample groups, which is of particular interest for high-temperature environments. Although samples made from HP500 (material B) had comparable conductivities at ambient conditions (298 K), these measurements significantly deviate with increasing temperature, resulting in a difference between conventional and LCM alumina of 26.1% for B, 25 μm and 57% for B, 50 μm at 373 K and 28% for B, 25 μm and 62% for B, 50 μm at 473 K.

In addition to characterizing the bulk properties, the thermal conductivity of a printed porous structure is also measured to quantify its dependence on the constituent material properties and geometry. The effective thermal conductivity of a sample printed from HP500 material with a layer thickness of 50 μm was measured and compared with simulation results, using the software PuMA.[27] The simulation results are within 5% of those measured at all temperatures, thereby confirming that the constituent material thermal conductivity and geometry (from μ-XCT) are adequate to predict the effective properties of a printed macroporous structure. The following equation is proposed to quantify this relationship

$$\lambda_{s,\text{eff}} = \alpha(1 - \epsilon)\lambda_s(T) \tag{8}$$

where $\lambda_{s,\text{eff}}$ is the effective thermal conductivity, α is a correction factor corresponding to the geometry ($\simeq 0.4$ for the D-surface structure), and $\lambda_s(T)$ is the temperature-dependent thermal conductivity of the constituent material (i.e., conventional or LCM). For the temperature range considered, 298 K $< T <$ 473 K, the following dependence is observed

$$\lambda_{s,\text{LCM}}(T) = aT^2 + bT + c \tag{9}$$

where a, b, and c for HP500 alumina is determined as 1×10^{-3} W m^{-1} K^{-3}, -0.87 W m^{-1} K^{-2}, and 200 W m^{-1} K^{-1},
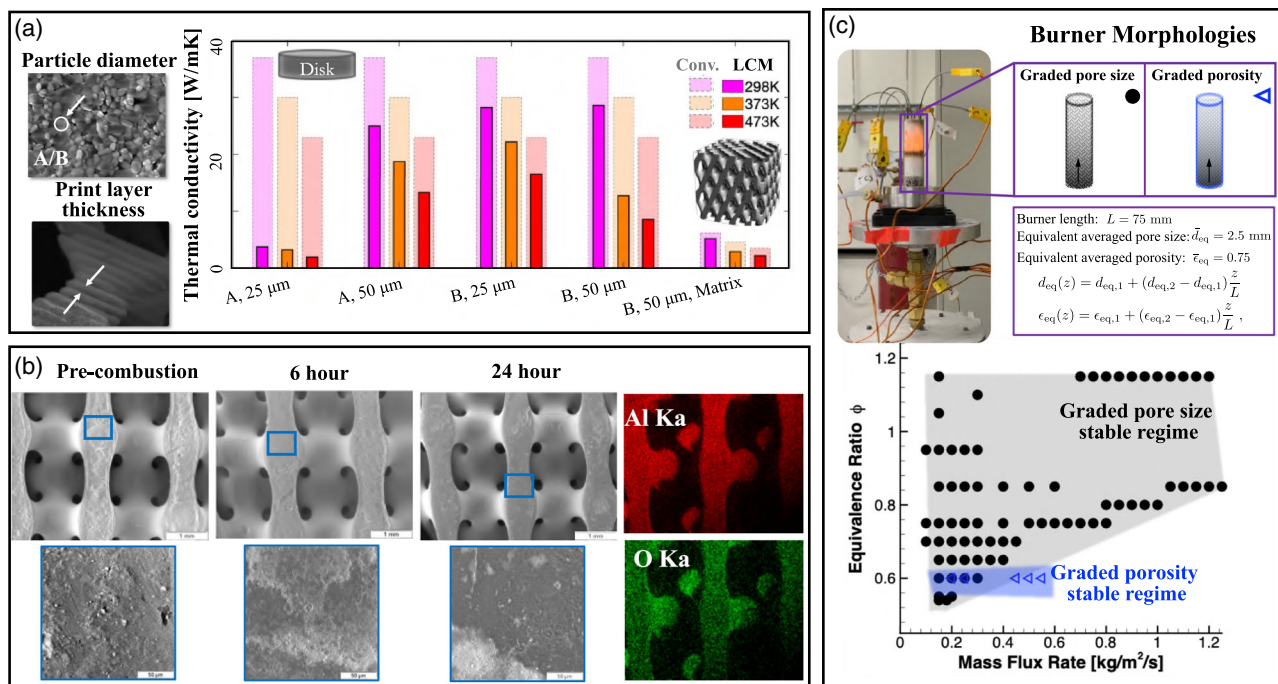
Figure 4. Post-print analysis of the thermal properties, durability, and combustion performance of printed alumina: a) thermal conductivity measurements at various temperatures of the solid disks and porous matrix (A: 350D, B: HP500) and print-layer thickness 25 and 50 µm. All data presented correspond to samples printed with x–y plane layer orientations, with thermal conductivity measured in the z-direction. To quantify effects imposed by the LCM-fabrication technique, the thermal conductivity of conventionally manufactured high-grade alumina (Equation (6)) is also shown; b) SEM images of the porous matrix before and after durability testing by exposing the surface of the macroporous ceramic matrix to a premixed flame (see Figure 2) at 2130 K, and EDX maps of aluminum and oxygen after the test; and c) interstitial combustion in PMBs of various morphologies along with corresponding flame stability regimes (see Table 1 for geometric parameters of macroporous matrices).

respectively. Using this expression, the effective conductivity using the constituent values from conventionally manufactured high-grade alumina (Equation (7)) is predicted and compared with that measured in the LCM-alumina matrix (final group of columns in Figure 4a). This analysis illustrates that, assuming adequate layer-to-layer adhesion, the LCM process reduces the effective conductivity in excess of 20%, as compared with other manufacturing techniques.

The thermostructural durability of the final sintered HP500 alumina porous matrix was examined next. For this, the macroporous ceramic surface was exposed to a hot combustion environment that was provided from a Bunsen flame. The matrix was mounted 3 mm above the burner exit, operated with methane at an equivalence ratio of $\phi = 0.9$ (see Phase III in Figure 2 for setup). At this operating condition, the flame temperature is $T = 2130$ K, and the equilibrium combustion-product composition consists of a mixture of $N_2:H_2O:CO_2:O_2:NO:OH:CO = 0.718:0.17:0.084:0.018:0.004:0.004:0.002$. Before the start of the test and after time intervals of 1, 6, and 24 h, the surface exposed to the flame was imaged using an XL30 environmental SEM. The SEM images after each interval illustrate that the material does not undergo any cracking or appreciable surface oxidation even after 24 h of exposure to the combustion environment, as shown in Figure 4b. Furthermore, the EDX did not show any chemical changes or contamination of the material, measuring a homogenous distribution of aluminum and oxygen elements

before and after the combustion experiments. Therefore, the manufacturing technique and matrix geometry proposed in this work are suitable for high-temperature applications and are stable in combustion environments.

To evaluate the potential performance enhancements enabled by tailoring of macroporous structures, these LCM-fabricated lattices were used in application to a PMB experiment. Compared with conventional free-flame systems, PMBs are characterized by significantly higher burning velocities, enhanced flame stabilization, and lower emissions of nitric oxides.[28–30]

Using the methodology outlined earlier, two porous structures with equivalent averaged pore size ($\bar{d}_{eq} = 2.5$ mm), equivalent averaged porosity ($\bar{\epsilon}_{eq} = 0.75$), length ($L = 75$ mm), and diameter ($D = 20$ mm) were designed, printed, and tested in a porous burner to characterize flame stability (i.e., a stationary temperature profile). The results from this experiment showed substantial sensitivity of the flame stabilization to the local morphology of the porous structure. This is shown in Figure 4c, showing a schematic of burner setup (see Experimental Section for further information) together with a measured combustion stability diagram. The stability diagrams shows stable operating region as a function of mass-flux rate and equivalence ratio. The shaded regions indicate stable operation. These results demonstrate the sensitivity of the burner to the macroporous matrix morphology. In particular, it can be seen that a significant extension of the stable operating conditions is achievable using a smoothly graded

pore-diameter matrix (gray shaded region) as compared with a graded porosity (blue shaded region). In the graded pore-diameter burner, the flame dynamically stabilizes in the matrix at different operating conditions and, thus, enables stable operation over a wider range of equivalence ratios. The methodology outlined in this work not only enables the validation of enhanced performance of a novel PMB design, but also demonstrates the significant impact that geometric tailoring can have on the functioning of thermofluid systems.

In this work, a framework is developed to enable the design and fabrication of tailored macroporous ceramic structures for application to high-temperature environments. This framework combines functionally graded TPMS-lattice structures and lithography-based AM. The fidelity of the LCM process in reproducing the input geometry was examined using XCT imaging, and durability analysis of the printed alumina samples both pre- and post-thermal exposure indicate negligible variation and, thus, demonstrate the chemical and physical stabilities of the printed material. Effects of the printing process on the thermal conductivity were examined, showing that the printing process (layer thickness, orientation, and adhesion) and sintering material directly affect the thermal conductivity. Selective control of these process parameters offers opportunities for the local modulation of thermal and structural properties of printed ceramic materials. In addition, 3D macroporous ceramic structures with specified axial porosity and pore-diameter variations were translated from computer models into physical samples. By considering applications to low-emission PMBs, the benefit of realizing tailored matrix morphologies in modulating the operating regime and power-dynamic range was demonstrated that were not achievable with conventionally manufactured porous foams. As such, the tailoring of the macroporous structure holds opportunities for application-specific designs and achieving significant improvements of the performance for other high-temperature thermofluid environments, such as catalytic converters, reformers, heat exchangers, or thermal protection materials. Future work will aim to incorporate corrections in the input geometry to enable high-fidelity prints using LCM as well as explore strategies to enhance the thermal shock resistance in these structures by applying the proposed framework for the design and fabrication of tailored macroporous structures to higher thermal-shock resistant ceramic materials, such as mullite and SiC.

Experimental Section

All interstitial combustion experiments in a PMB were performed using a methane/air mixture at atmospheric pressure. The printed porous samples were wrapped in insulation and housed in a quartz tube. The burners were placed above a bed of packed stainless steel beads that served as a flashback arrestor. Flow rates of reactants were measured and controlled using Alicat Scientific mass flow controllers (MFCs). Compressed air and methane flows were mixed at a tee junction of ≈200 tube diameters upstream of the burner to achieve a homogeneous mixture prior to entry into the burner. Six K-type mineral-insulated thermocouples were placed along the axial profile of the burner at azimuthal locations varying by 60°. Temperature measurements were primarily used to determine flame location and stability. Errors reported by the manufacturer were ±1% of the measured value for the MFCs and ±0.75% of the measured value for the thermocouples. Stable operation was defined as continuous operation without changes in thermocouple measurements greater than 5 K over

5 min. After each stable operating condition was determined, the mass flux was changed to find the maximum stable flow rate for each equivalence ratio. The blow-off limit was determined first by the occurrence of the maximum temperature measurement at the thermocouple furthest downstream, and subsequently by the continual decrease in temperature measured by this thermocouple. Flashback was determined similarly, except that the maximum temperature was observed at the thermocouple furthest upstream, followed by a decrease in temperature of its adjacent thermocouple.

Conflict of Interest

The authors declare no conflict of interest.

[1] A. Sommers, Q. Wang, X. Han, C. T. Joen, Y. Park, A. Jacobi. *Appl. Therm. Eng.* **2010**, *30*, 1277.

[2] A. J. Onstad, C. J. Elkins, F. Medina, R. B. Wicker, J. K. Eaton. *Exp. Fluids* **2011**, *50*, 1571.

[3] U. Scheithauer, E. Schwarzer, G. Ganzer, A. Kornig, W. Becker, E. Reichelt, M. Jahn, A. Hartel, H. Richter, T. Moritz, A. Michaelis, *Micro-Reactors Made by Lithography-Based Ceramic Manufacturing (LCM)*, John Wiley & Sons, Ltd, Hoboken, NJ **2016**, pp. 31–41.

[4] U. Scheithauer, E. Schwarzer, T. Moritz, A. Michaelis. *J. Mater. Eng. Perform.* **2018**, *27*, 14.

[5] D. Trimis, in *Proc. of the Fluids 2000 Conf. and Exhibit*, American Institute of Aeronautics and Astronautics, Reston, VA **2000**, 2298.

[6] J. Binner, *Ceramics Foams*, John Wiley & Sons, Ltd., Hoboken, NJ **2006**, pp. 31–56.

[7] A. R. Studart, U. T. Gonzenbach, E. Tervoort, L. J. Gauckler, *J. Am. Ceram. Soc.* **2006**, *89*, 1771.

[8] G. Bianchi, S. Gianella, A. Ortona, *J. Ceram. Sci. Technol* **2017**, *8*, 59.

[9] M. Schwentenwein, J. Homa, *Int. J. Appl. Ceram. Technol.* **2015**, *12*, 1.

[10] G. Mitteramskogler, R. Gmeiner, R. Felzmann, S. Gruber, C. Hofstetter, J. Stampfl, J. Ebert, W. Wachter, J. Laubersheimer, *Addit. Manuf.* **2014**, *1–4*, 110.

[11] I. Maskery, L. Sturm, A. Aremu, A. Panesar, C. Williams, C. Tuck, R. Wildman, I. Ashcroft, R. Hague, *Polymer* **2018**, *152*, 62.

[12] S. Rajagopalan, R. A. Robb, *Med. Image Anal.* **2006**, *10*, 693.

[13] F. P. Melchels, K. Bertoldi, R. Gabbrielli, A. H. Velders, J. Feijen, D. W. Grijpma, *Biomaterials* **2010**, *31*, 6909.

[14] F. P. W. Melchels, A. M. C. Barradas, C. A. van Blitterswijk, J. de Boer, J. Feijen, D. W. Grijpma, *Acta Biomater.* **2010**, *6*, 4208.

[15] H. A. Schwarz, *Gesammelte mathematische Abhandlungen*, Vol. *1*, J. Springer, Berlin **1890**.

[16] A. H. Schoen. Technical Report Technical Note No. D-5541, U.S. National Aeronautics and Space Administration, Washington, DC **1970**.

[17] S. Sobhani, D. Mohaddes, E. Boigne, P. Muhunthan, M. Ihme, *Proc. Combust. Inst.* **2019**, *37*, 5697.

[18] *Multi-Parametric Programming: Theory, Algorithms and Applications* (Eds: E. N. Pistikopoulos, M. C. Georgiadis, V. Dua), Wiley-VCH, Weinheim **2007**.

[19] S. Sobhani, P. Muhunthan, E. Boigne, D. Mohaddes, M. Ihme, unpublished.

[20] J. C. Wang, H. Dommati, S. J. Hsieh, *Int. J. Adv. Manuf. Technol.* **2019**, *103*, 2627.

[21] G. Mitteramskogler, R. Gmeiner, R. Felzmann, S. Gruber, C. Hofstetter, J. Stampfl, J. Ebert, W. Wachter, J. Laubersheimer, *Addit. Manuf.* **2014**, *1*, 110.

[22] E. Schwarzer, M. Götz, D. Markova, D. Stafford, U. Scheithauer, T. Moritz. *J. Eur. Ceram. Soc.* **2017**, *37*, 5329.

[23] D. Legland, I. Arganda-Carreras, P. Andrey. *Bioinformatics* **2016**, *32*, 3532.

[24] E. Maire, P. Colombo, J. Adrien, L. Babout, L. Biasetto. *J. Eur. Ceram. Soc.* **2007**, *27*, 1973.

[25] N. Mathis. *High Temperatures High Pressures(UK)* **2000**, *32*, 321.

[26] P. Auerkari, *Mechanical and Physical Properties of Engineering Alumina Ceramics*, Technical Research Centre of Finland Espoo, Espoo **1996**.

[27] J. C. Ferguson, F. Panerai, A. Borner, N. N. Mansour. *SoftwareX* **2018**, *7*, 81.

[28] D. Trimis, F. Durst, *Combust. Sci. Technol.* **1996**, *121*, 153.

[29] G. Brenner, K. Pickenäcker, O. Pickenäcker, D. Trimis, K. Wawrzinek, T. Weber, *Combust. Flame* **2000**, *123*, 201.

[30] S. Wood, A. T. Harris, *Prog. Energ. Combust. Sci.* **2008**, *34*, 667.